Simultaneous time-space resolved reflectivity and interferometric measurements of dielectrics excited with femtosecond laser pulses

M. Garcia-Lechuga,[1,*] L. Haahr-Lillevang,[2] J. Siegel,[1] P. Balling,[2] S. Guizard,[3] and J. Solis[1,†]

[1]*Laser Processing Group, Instituto de Optica, Consejo Superior de Investigaciones Científicas (IO-CSIC), Serrano 121, 28006-Madrid, Spain*

[2]*Department of Physics and Astronomy, Aarhus University - DK-8000 Aarhus C, Denmark*

[3]*Laboratoire des Solides Irradiés/Commissariat à l'Energie Atomique (CEA), Institut Rayonnement-Matière de Saclay (IRAMIS), Ecole Polytechnique–Palaiseau, France*

(Received 23 December 2016; revised manuscript received 25 May 2017; published 27 June 2017)

Simultaneous time-and-space resolved reflectivity and interferometric measurements over a temporal span of 300 ps have been performed in fused silica and sapphire samples excited with 800 nm, 120 fs laser pulses at energies slightly and well above the ablation threshold. The experimental results have been simulated in the frame of a multiple-rate equation model including light propagation. The comparison of the temporal evolution of the reflectivity and the interferometric measurements at 400 nm clearly shows that the two techniques interrogate different material volumes during the course of the process. While the former is sensitive to the evolution of the plasma density in a very thin ablating layer at the surface, the second yields an averaged plasma density over a larger volume. It is shown that self-trapped excitons do not appreciably contribute to carrier relaxation in fused silica at fluences above the ablation threshold, most likely due to Coulomb screening effects at large excited carrier densities. For both materials, at fluences well above the ablation threshold, the maximum measured plasma reflectivity shows a saturation behavior consistent with a scattering rate proportional to the plasma density in this fluence regime. Moreover, for both materials and for pulse energies above the ablation threshold and delays in the few tens of picoseconds range, a simultaneous "low reflectivity" and "low transmission" behavior is observed. Although this behavior has been identified in the past as a *signature* of femtosecond laser-induced ablation, its origin is alternatively discussed in terms of the optical properties of a material undergoing strong isochoric heating, before having time to substantially expand or exchange energy with the surrounding media.

DOI: 10.1103/PhysRevB.95.214114

I. INTRODUCTION

Since the first experiments regarding the interaction of femtosecond (fs) laser pulses with dielectric materials [1,2], the fundamental mechanisms of carrier excitation and relaxation have been a subject of intensive research. Indeed, while comprehension of these processes has been largely improved by theoretical work and modeling [3–6], several aspects of the carrier dynamics are still controversial. In particular, the role and relative importance of impact ionization during the material excitation as a function of the exciting pulse duration is still debated, and many research papers stressing its importance [7–11] or the opposite [12,13] can be found in the literature. Part of the problem comes from the difficulties in comparing the results of different experimental techniques aimed at determining the temporal evolution of the excited carrier population. These methods are, with exceptions [14], either sensitive to the real part of the complex refractive index (i.e., transient interferometric methods that evaluate the phase shift experienced by a probe pulse [15,16]) or to its imaginary part (transient reflectivity, transmission, or absorption measurements [17,18]). However, in many cases these measurements lack spatial resolution, which makes it difficult to evaluate the actual local fluence triggering different processes.

Similarly, the role of the formation of self-trapped excitons (STEs) [15] as a carrier relaxation mechanism for near-and-above ablating fluences is still under debate. STE formation is a well-established relaxation mechanism, especially in materials with a small elastic constant, like fused silica and alkali halides [19], where excitons are strongly bound and localized near a single atom [20]. STE formation has been shown by means of time-resolved interferometry measurements to very efficiently reduce the optical signature of free electrons over a time span of the order of 500 fs for fluences up to the ablation threshold in fused silica [15,19,21]. However, a number of papers have reported time-resolved reflectivity or transmission measurements of the excited material for fluences above the ablation threshold showing carrier population buildup and relaxation times much slower than those observed in interferometry experiments [22–25]. Among these, those using spatially resolved measurements (fs-resolved imaging) provide information about the plasma density evolution as a function of the local fluence and apparently support that, for high plasma densities (close to $10^{22}\,\mathrm{cm}^{-3}$) showing a substantial local reflectivity increase, the formation of STEs is not the dominant carrier relaxation mechanism. This different behavior has been related to Coulomb screening effects [25] at large carrier densities, although other factors might as well contribute to different exciton dynamics at the surface. The discrepancies observed between reflectivity and interferometric measurements could also be due to the larger thickness probed with the interferometry method: the contribution from the thin, highly excited ablating layer could be hidden by a larger contribution from the bulk in the interferometry experiments.

In general, the comparison of experiments in which plasma density evolution is evaluated is difficult due to the lack of spatial resolution in most experimental layouts, which impedes assessing the actual local excitation fluence associated with a

*garcialechuga.mario@gmail.com
†j.solis@io.cfmac.csic.es

 ©2017 American Physical Society

given carrier density. Additionally, the sensitivity of different experimental configurations to the plasma density depends on the probe wavelength, the pump-to-probe beam size ratio (in setups lacking spatial resolution), or the temporal resolution of the measurement system. In fact, the magnitude of the electron densities that are to be measured also has an impact on the sensitivity of the measurement setup: the reflectivity changes associated with the evolution of the free carrier density are much stronger in the vicinity of the so called *critical* plasma density (when the density of free carriers brings the material to a strongly absorbing, metallike state at the probe wavelength). Additionally, the estimation of the plasma density using the Drude model depends on several parameters which are normally unknown and need to be assumed *a priori*, like the carrier-carrier scattering rate and its density dependence or the effective electron mass [26,27].

This paper aims to shed some light on part of the above-mentioned controversies by reporting results of simultaneous spatially and temporally resolved reflectivity, interferometric, and absorption measurements obtained upon excitation of fused silica and sapphire with fs laser pulses at fluences slightly and well above the ablation threshold. These materials show very different relaxation behaviors upon fs laser excitation below the ablation threshold, which has been attributed to the formation of STEs in the case of silica [13,19], not present in sapphire. The time-resolved measurements have been complemented by simulations of the carrier density evolution based on a modified multiple-rate equation (MRE) model [28] in order to obtain information about different material parameters relevant for the carrier dynamics.

II. EXPERIMENTAL DETAILS

The experiments were performed at the LUCA laser facility in the Saclay Laser-Matter Interaction Center (SLIC) of the CEA. Figure 1 shows a scheme of the experimental setup including the excitation of the sample and the space-and–time-resolved simultaneous measurement of the surface reflectivity of the sample as well as the absorption and phase shift experienced by a transmitted probe pulse. The samples used in the experiments were polished $10 \times 10 \times 1.5$ and $10 \times 10 \times 1\,\mathrm{mm}^3$ blocks of fused silica (amorphous silicon dioxide, ultraviolet grade) and single crystal sapphire from SurfaceNet, respectively. The samples were irradiated at normal incidence, with the beam propagation axis parallel to the c axis in the case of sapphire. The nominal bandgaps are 8.9 eV and 9.9 eV, respectively, for fused silica and sapphire.

The laser is a chirped-pulse amplification (CPA) [29] Ti–sapphire system delivering fs pulses up to 70 mJ at 800 nm, with a repetition rate of 20 Hz. The beam entering the setup is split into two arms with a beam splitter (BS1) to generate the pump and probe laser pulses for the time-resolved measurements. The pump beam (Arm1, 800 nm central wavelength, 120 fs pulse duration (FWHM) at the sample location) passes through a mechanical shutter to enable single pulse exposures and several optical elements to control its energy, before being focused at normal incidence on the sample employing a lens (L1, $f = 300\,\mathrm{mm}$ focal length). The sample is moved after a given region has been exposed to a single pump pulse in order to avoid cumulative damage effects. In the probe beam

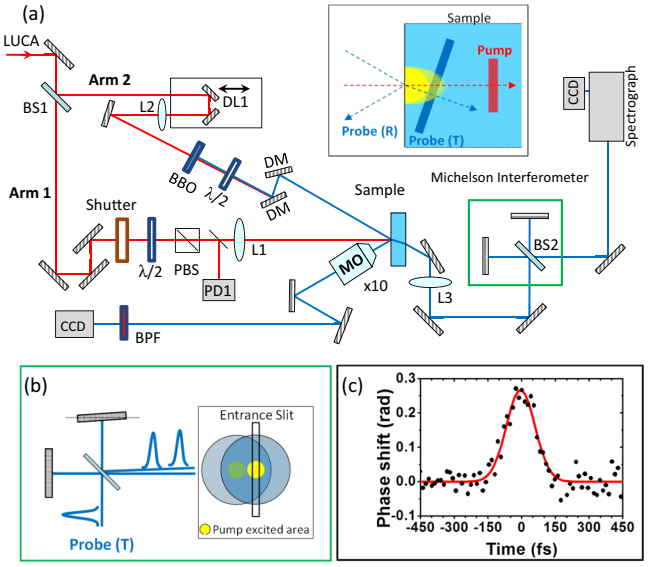

FIG. 1. (a) Scheme of the experimental setup for simultaneous measurement of the sample surface reflectivity and the intensity and phase shift changes experienced by a transmitted probe pulse. BS, beam splitter; L, lens; DL1, variable optical delay line; BBO, frequency-doubling crystal; λ/2, lambda/half-wave plate; DM, dichroic mirror; PBS, polarizing beam splitter; PD1, Photodiode for pulse energy monitoring; MO, long-working-distance microscope objective; CCD, charge-coupled device camera; BPF, bandpass filter. The inset shows a simplified scheme of the regions interacting with the pump and probe pulses and their propagation (R: reflected beam, T: transmitted beam). (b) Scheme of the interferometric arrangement in the Michelson interferometer. The two beams are shifted and delayed so as to generate an interferogram with the contributions of the nonexcited region and the central part of the pump-excited region. The spectrograph slit axis is vertical. (c) Third-order autocorrelation trace of the 800 nm pump pulse at the sample location, consistent with a pulse duration of 120 fs (FWHM).

arm (Arm2) a variable delay line (DL1) allows controlling the relative delay between pump and probe pulses. After the delay line, the probe beam passes through a lens (L2, $f = 1\,\mathrm{m}$ focal length) and half-wave plate (λ/2) to be frequency doubled using a beta barium borate (BBO) crystal. The energy of the probe pulse is typically 1–10 μJ and its duration 115 fs. The use of a probe beam at 400 nm enables a better spatial resolution for transient reflectivity measurements and enables spectral discrimination from pump-beam scatter. In some cases (i.e., determination of pump pulse duration), the fundamental frequency was used both for pumping and probing. A λ/2 wave plate in the probe beam path enables the selection of the polarization of the probe beam reaching the surface.

For the reflectivity measurements, the layout is similar to that reported in Refs. [23,24,30]. The probe pulse, incident on the surface at an angle of 30° to the sample normal, is used as the illumination source of a microscope imaging system formed by a 10× (0.26 numerical aperture [NA]) long working distance microscope objective (MO), and a charge-coupled device (CCD) camera, using a bandpass filter (BPF) in order to record only the reflectivity evolution at the probe wavelength. The use of an imaging configuration enables acquiring the reflectivity evolution at different positions and thus local

fluences, given the Gaussian profile of the excitation beam [30,31]. Two different images are acquired for each delay, one corresponding to the region of interest before irradiation and the other corresponding to the specified delay between the pump and the probe pulses. The image before irradiation is used as a reference to determine the relative reflectivity changes for each delay, as $R_{\mathrm{rel}} = R(\tau)/R_0$, where $R(\tau)$ is the transient surface reflectivity for a given delay after excitation, and R_0 is the reflectivity of the nonexcited surface. The angled incidence of the probe causes the reflections at the top front and bottom surfaces of the sample to be sufficiently separated to enable blocking the unwanted reflection from the back surface before reaching the imaging device. Additionally, it was carefully checked that no signal was detected in absence of the probe pulse, even for the highest fluences used. Such signal could arise from scattered second harmonic radiation generated by the pump pulse (hyper-Rayleigh scattering [32]). Its presence would be obvious for negative delays (when the probe pulse arrives at the surface before the pump pulse). No indications of this effect have been observed.

For the interferometry measurements, the probe beam transmitted through the sample [see the inset of Fig. 1(a)] enters a Michelson interferometer as described in detail elsewhere [13,19]. Briefly, the interferometer, as schematically shown in Fig. 1(b), is aligned in such a way that the part of the beam traversing the laser-excited region is temporally delayed and overlapped with a part of the beam traversing a nonirradiated region. A third lens (L3, $f = 175$ mm) is used to image the two overlapped beams onto the entrance slit of an imaging spectrometer in which they are interfered in the frequency domain. The resulting fringe pattern is recorded by a CCD camera. For a given delay, two interference images are acquired, with and without the pump pulse (reference image). A line-wise Fourier transform (FT) of these images is then performed giving access to the phase and amplitude along the vertical axis. The induced phase change is then computed as the difference between the phase of the line-wise FTs of the "pump" and "no-pump" interferograms, while the overall transmittance is calculated from the ratio of the amplitudes of the FTs. The phase shift is caused by the modification of the real part of the refractive index in the probed volume, while the amplitude is affected by changes in reflectivity and absorption. Due to the close relationship between transmittance and the evolution of the imaginary part of the refractive index, and in order to use a notation consistent with previous works, we will use the term *absorption* to refer to the ratio of the power spectra of the interferograms with and without the pump. The spatial region analyzed is located at the center of the excited zone and enables a comparison of the transient phase and absorption with the transient reflectivity images. It is worth noting that the interferometric approach used here is different from that used in Ref. [33] and similar layouts, where the Michelson interferometer is placed before the sample and, hence, the pump-probe delay span accessible is limited by the separation of the two probe pulses.

For a weak excitation pulse, the phase changes induced by the excitation pulse are caused by the intensity dependence of the material refractive index (Kerr effect). This facilitates the determination of the zero-delay temporal reference in the time-resolved optical measurements, which is taken at the maximum of the *Kerr signal*. This also enables determining the pulse duration at the sample location since the temporal envelope of the Kerr signal is in itself a third-order autocorrelation [34] (pump and probe lasers at 800 nm) or cross-correlation (pump at 800 nm and probe at 400 nm) of the pulse. From the fit of the autocorrelation trace of the pulse [Fig. 1(c)], assuming a temporally Gaussian pulse shape, the pulse duration determined at 800 nm is 120 ± 10 fs (FWHM; third-order autocorrelation factor of 1.22 [34]).

Finally, the spot size of the pump beam at the surface, as well as the ablation threshold fluence of the two materials at 800 nm, for 120 fs laser pulses were determined by analyzing the evolution of the ablation crater diameter, as measured by optical microscopy, as a function of the pulse energy using a Liu-type plot [35]. The obtained spot size was 98 μm ($1/e^2$ diameter) and the ablation thresholds determined were $F_{\mathrm{th}} = 3.7\,\mathrm{J/cm^2}$ and $F_{\mathrm{th}} = 4.6\,\mathrm{J/cm^2}$ for fused silica and sapphire, respectively. In sapphire, it has to be considered that the indicated threshold corresponds to the strong ablation regime [36] with crater depths of several tens of nanometers. Gentle ablation [37], caused by Coulomb explosion, is observed for lower fluences, above $3.8\,\mathrm{J/cm^2}$, with crater depths of just a few nanometers. From now on, the fluence values indicated in the text will be referenced to the indicated threshold value for each material.

III. MODELING

The experimental results have been modeled using a MRE model, as originally proposed in Rethfeld and others [4,7], with several extensions [38]. The conduction band (CB) is divided into discrete energy levels separated by the photon energy, and the valence band (VB) and the trapped exciton level are described by a single energy level, as shown in the schematic of Fig. 2(a). The maximum density of excitons is set to one per unit cell. The time-dependent density of electrons in each

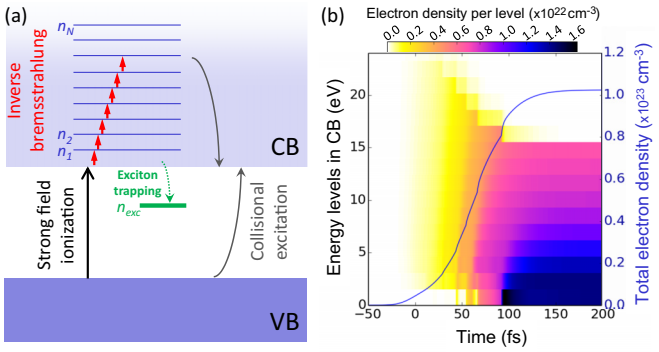

FIG. 2. (a) Scheme of the processes leading to changes in the density and energy of electrons, including the relevant optically induced transitions. (b) Temporal evolution of the electron distribution in the CB as calculated using the MRE model for the case of sapphire, for a pulse duration of 120 fs (FWHM); the pulse central wavelength is 800 nm and the pulse fluence is $1.60 \times F_{\mathrm{th}}$. The electron trapping mechanism, shown in panel (a) is not present in sapphire. The time scale zero point is taken at the maximum intensity of the pump pulse. The color scale indicates the electron density of the different energy levels. The total electron density as a function of time is shown as a blue line, with the corresponding scale displayed in the right vertical axis.

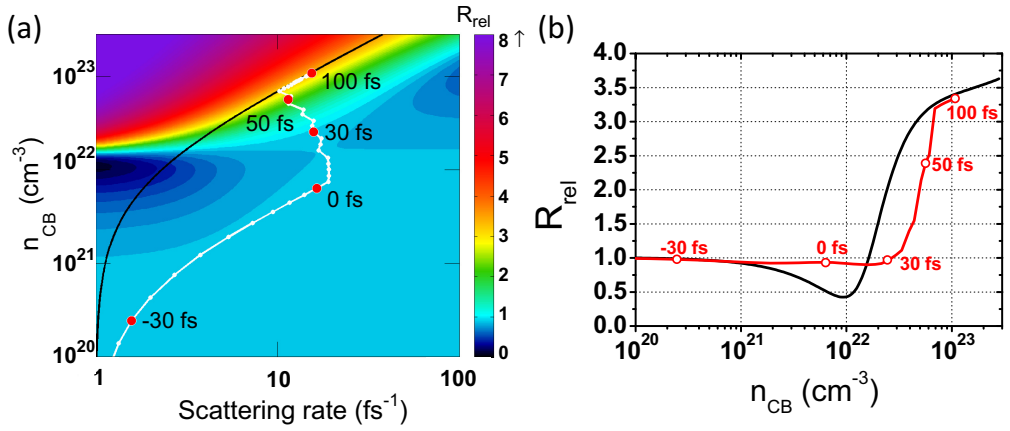

FIG. 3. (a). Relative reflectivity at 400 nm and 30° angle of incidence (normalized to that of the unperturbed material, $R_{\text{rel}} = 1$) for s-polarization in sapphire as a function of the density of CB (n_{CB}) electrons and the scattering rate (Γ) using the Drude model and Clausius-Mossotti correction [Eq. (1)]. The corresponding color code scale is given at the right side. The white dots correspond to the n_{CB} and Γ values calculated with the MRE model at the indicated delays relative to the peak intensity of the pump pulse, upon excitation with a 120 fs pulse (FWHM) at 800 nm and a pulse fluence of $1.60 \times F_{\text{th}}$. The temporal separation between the white dots is 3.3 fs. The red dots indicate characteristic temporal positions of the carrier density evolution (see text). The evolution as a function of time of the kinetic energy distribution and the total electron density in similar excitation conditions is shown in Fig. 2(b). The black line corresponds to the reflectivity evolution for a scattering rate directly proportional to the density plus a constant factor (see text). (b) Relative reflectivity as a function of n_{CB} calculated according to the MRE model (red line) and assuming a scattering rate directly proportional to the density plus a constant factor (black line), the latter showing the characteristic minimum associated with the so-called critical electron density. The characteristic temporal positions of the carrier density evolution according to the MRE model have been similarly indicated.

level is calculated by numerically solving a set of coupled rate equations containing: strong-field ionization from the VB in the Keldysh description, heating of CB electrons by inverse bremsstrahlung, collisional impact excitation, and trapping of electrons into the exciton level in the case of fused silica. In the case of sapphire, relaxation via STE formation has not been reported, a behavior which has been related to its large elastic constant [19]. The model includes the propagation of light into the material by considering the absorption in discretized layers of the material due to the combined effect of strong-field absorption and the absorption in the CB electron plasma [39]. Figure 2(b) shows as an illustrative example of the information accessible through the MRE model. It shows the temporal evolution of the electron distribution calculated for excitation in sapphire with a 120 fs pulse (FWHM) at 800 nm and a pulse fluence of $1.60 \times F_{\text{th}}$ (excitation conditions similar to those in Fig. 3). The discretized energy levels of the CB used in the model are clearly visible. The CB electron population increases strongly near the peak of the pulse, where strong-field excitation initiates the dynamics. Simultaneously, inverse bremsstrahlung heats the excited electrons, as can be seen by the population extending to high kinetic energies. During the trailing edge of the pulse, and even after the pulse is over (>50 fs), collisional excitation leads to additional CB electron generation while simultaneously cooling the high-energy electrons. The integral over the different kinetic energy values (total electron density) has also been included in the figure.

The optical response of the material is governed by the complex refractive index, $\tilde{n}^2 = (n + i\kappa)^2$ which is modeled using a Drude-Lorentz model of the dielectric function, $\varepsilon(\omega)$.

$$\tilde{n}^2 = \varepsilon = \varepsilon_b - \frac{\omega_{\text{pl}}^2}{\omega_l^2 + i\omega_l\Gamma} + f_{\text{exc}}\frac{\omega_{\text{exc}}^2}{\omega_l^2 - \omega_0^2 + i\omega_l\Gamma_{\text{exc}}} \quad (1)$$

where the first term, ε_b, is dependent on the density of VB electrons and becomes 1 in the limit of an empty VB and equal to the square of the unperturbed refractive index in the limit of no excitation through the Clausius-Mossotti relation [40]. The term $\omega_{\text{pl}}^2 = e^2 n_{\text{CB}}/m_{\text{con}}\epsilon_0$ is the plasma frequency of the free electrons in the CB that reaches the so-called critical value when it equals the frequency of the laser ($n_{\text{crit}} = \epsilon_0 m_{\text{con}}\omega^2/e^2$), e is the electron charge, n_{CB} is the free electron density, m_{con} is the effective mass of the electrons distributed throughout the CB, and ϵ_0 is the vacuum permittivity. In the denominator of Eq. (1), ω_l is the laser frequency and Γ is the free electron scattering frequency. The determination of the material reflectivity at a given angle of incidence can be obtained straightforwardly for known values of the free carrier density (n_{CB}) and the scattering frequency (Γ) by using Eq. (1) combined with the Fresnel equations.

In the model used, Γ has two contributing factors, $\Gamma = \Gamma_{\text{e-ph}} + \Gamma_{\text{carrier-carrier}}$, where $\Gamma_{\text{e-ph}}$ is a constant electron-phonon scattering rate and $\Gamma_{\text{carrier-carrier}}$ [41] is in general an electron-temperature-dependent factor, calculated from a semiclassical collision model of hard spheres and limited for low excitation through a truncation of the effective electron radius [27,28]. In the high density limit where the collective temperature is low due to collisional cooling, $\Gamma_{\text{carrier-carrier}}$ is limited by the Fermi speed limit of the electrons, effectively creating a density-dependent scattering rate, similar to expressions of the scattering rate used in several papers, including Refs. [24,26]. The third term in Eq. (1) models the STE optical signature. In the numerator there is an exciton density-dependent term $\omega_{\text{exc}}^2 = e^2 n_{\text{exc}}/m_{\text{exc}}\epsilon_0$. The f_{exc} is the exciton oscillator strength, ω_0 is the oscillator energy level, and Γ_{exc} is a constant exciton scattering rate.

TABLE I. Model parameters used in the simulations [38,48]. No scaling of the Keldysh ionization rate has been used. The STE oscillator level ω_0, in parentheses is used at the surface, as discussed in connection with the data. The $\Gamma_{\text{carrier-carrier}}$ scaling indicates the scaling factor for the density- and temperature-dependent carrier-carrier scattering calculated from a semiclassical expression [27].

	Bandgap (eV)	$\Gamma_{\text{e-ph}}$	$\Gamma_{\text{carrier-carrier}}$ scaling	α_{col}	m_{con}	m_{val}	τ_{trap} (fs)	ω_0 (eV)	Γ_{exc} (eV)	f_{exc}	n_{val}
Al_2O_3	9.9	$1 \times 10^{15}\ s^{-1}$	1	$10^{15}\ s^{-1}$	0.38	3.99	N/A[a]	N/A	N/A	N/A	$2.8 \times 10^{29}\ m^{-3}$
SiO_2	8.9	$2 \times 10^{15}\ s^{-1}$	2	$10^{15}\ s^{-1}$	0.5	3	150	5.2 (3.8)	1.5	1	$3.2 \times 10^{29}\ m^{-3}$

[a]Not applicable.

The material parameters used for modeling are included in Table I. For sapphire, we have used an effective mass of $0.38\,m_e$ [19] when calculating the Keldysh strong-field ionization. However, an effective electron mass of $0.8\,m_e$ has been used in the Drude model calculations. This is justified by the fact that Keldysh excitation brings electrons to the bottom of the CB, where the curvature is large, leading to $0.38\,m_e$, while the highly excited electrons of the Drude model are less affected by the curvature of the band. In the simulations for fused silica, we used a value $0.5\,m_e$ [42], both when calculating the Keldysh excitation and the optical response with the Drude model, although values ranging $0.5\,m_e$ to $1.0\,m_e$ [4,43] can be found in the literature.

Figure 3(a) shows the relative reflectivity (normalized to that of the unperturbed material, $R_{\text{rel}} = 1$) of sapphire as a function of the electron density and scattering rate using Eq. (1) and the Fresnel relations for an incidence angle of 30°. The color scale in the figure shows the relative reflectivity calculated with Eq. (1) as a function of n_{CB} and Γ without any restriction for the relation between both parameters. The evolution of the reflectivity calculated according to the MRE model upon excitation with an 800 nm laser pulse of 120 fs (FWHM) with an energy of $1.6 \times F_{\text{th}}$ is shown as a white segmented line trajectory in the same figure [see also Fig. 2(b)]. The values of the white dots have been computed by determining the corresponding carrier densities (n_{CB}) and temperature-dependent scattering rates (Γ) with the MRE model for a given temporal delay. From these values, using Eq. (1) to determine the complex refractive index and the Fresnel equations, the reflectivity at the corresponding angle of incidence and polarization is calculated. The reflectivity evolution calculated with the MRE model has some interesting implications.

At approximately −30 fs (relative to the peak intensity of the pulse), both the electron density and scattering rate are still low, as seen in Fig. 3(a) [also, Fig. 3(b) relative reflectivity is ∼1]. Then both parameters increase because of simultaneous strong-field excitation and heating of electrons due to inverse Bremsstrahlung. Approximately at the peak of the pulse (∼0 fs), collisional excitation starts to set in, and the scattering rate begins to saturate and starts to slowly decrease (∼30 fs) while the electron density strongly increases. As an ensemble, the electrons are cooled by the collisional excitation of VB electrons into the CB. During this time, the reflectance is seen to go through a region between two adjacent minima [see also Fig. 3(b)]. During the pulse tail, at ∼50 fs, the white line is seen to first move to higher reflectance values and then bends towards higher scattering rate and density. This is due to the Fermi velocity limit effectively preventing the electrons from cooling further, while the density still rises through collisional excitation. The resulting reflectivity in this regime (>50 fs) begins to saturate, lying close to a contour of constant reflectance. This saturation effect is still not totally visible in Fig. 3(b).

The result of the MRE-based determination of the reflectivity evolution can be compared with a much simpler model using a scattering rate consisting of a constant term plus a density-dependent term: $\Gamma = \Gamma_{\text{e-ph}} + \Gamma_{\text{carrier-carrier},0} \times \frac{n_{\text{CB}}}{n_{\text{crit}}}$ with $\Gamma_{\text{e-ph}} = 10^{15}\ s^{-1}$ and $\Gamma_{\text{carrier-carrier},0} = 0.7 \times 10^{15}\ s^{-1}$. The corresponding reflectivity evolution corresponds to the smooth trajectory drawn as a black line in Fig. 3(a). This line is seen to pass through a reflectivity minimum at a CB electron density of $\sim 10^{22}\ cm^3$

The projection of both trajectories (MRE model and scattering rate proportional to carrier density plus a constant factor) on the reflectivity-density plane is plotted in Fig. 3(b). In this latter case, the reflectivity of the electron plasma shows a minimum, followed by a strong reflectivity increase. The transition from the light-transmitting to the strongly reflecting (and absorbing) behavior of the plasma has often been identified with the point at which the plasma reaches the critical density, n_{crit}. The reflectivity of the plasma at the critical density is only a few percent [44], and its skin depth on the order of the wavelength [1]. At slightly higher plasma densities, however, the material behaves transiently like a metal, showing simultaneously a high reflectivity and a very strong absorption in a thin layer where the nonreflected light is absorbed [1]. Due to the associated absorbance increase, reaching the critical density is also sometimes used as an indicator of laser-induced damage upon excitation.

In the results of the MRE model used, no dip is observed in Fig. 3, and, more importantly, the electron density above which the reflectivity starts to increase is shifted to higher electron densities. In what follows, it is worth noting that the simulated reflectivity values have been calculated by determining the corresponding excited carrier densities and scattering frequencies using the MRE model and using Eq. (1) to determine the complex refractive index for a given temporal delay after excitation. In order to ease the description of the experimental results, we will use the terms *under-critical* or *over-critical densities* when referring to a nearly transparent or strongly absorbing (reflecting) plasma at the probing wavelength, respectively. The reason for this is that although the *critical density* has no specific physical meaning in the context of the MRE model, strong changes in the reflectivity occur for carrier densities close to this value and also because the critical density is a parameter often used when comparing reflectance studies performed under different angles and wavelengths [26].

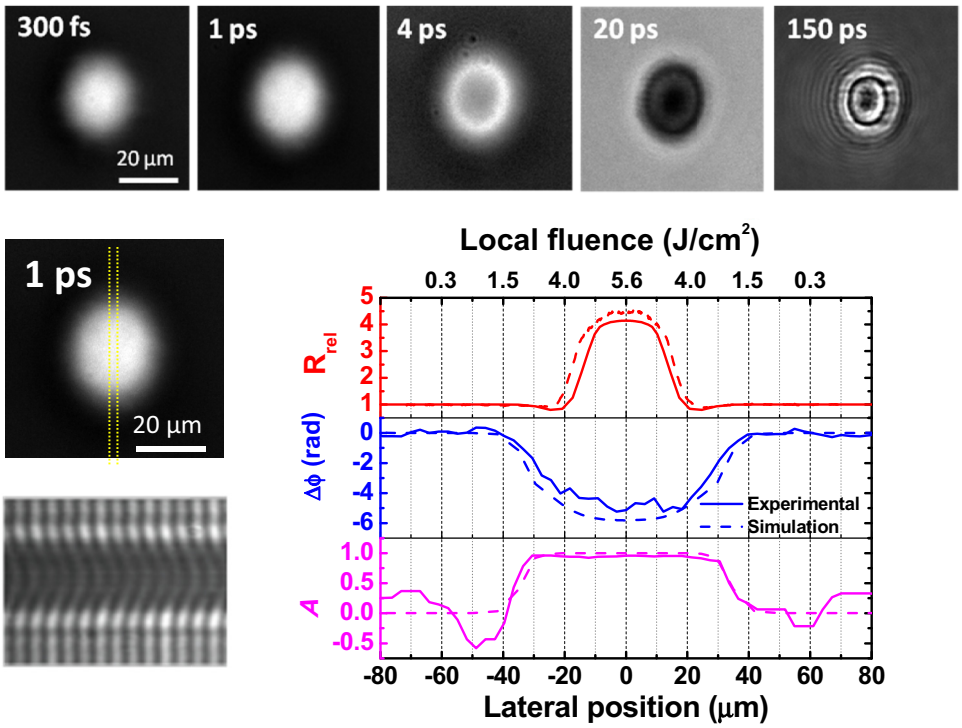

FIG. 4. (Upper row) Normalized reflectivity images ($R_{\rm rel} = R(\tau)/R_0$) at the indicated delays (τ) (R_0, reflectivity of the nonexcited surface) recorded upon excitation of sapphire with a fs laser pulse at a maximum fluence of 5.6 J/cm^2 at 800 nm. The contrast of the images has been adjusted individually to highlight the specific relevant reflectivity features in the corresponding timescale. The probe beam (400 nm) is p-polarized. (Left column) Reflectivity image for a delay of 1 ps in the same experimental conditions at larger magnification and typical interferometric image in transmission showing the fringe distortion caused by the phase shift. The cross sections corresponding to the measured relative reflectivity ($R_{\rm rel}$), phase change ($\Delta\phi$), and absorption (A) (see text) as a function of the vertical coordinate are plotted on the right (continuous lines). The dashed lines have been numerically calculated (see text).

IV. RESULTS AND DISCUSSION

Figure 4 shows, as an illustrative example, a set of fs-resolved microscopy images of the laser-excited sapphire surface for several time delays. The figure also includes an additional pair of reflectivity and interferometric images taken for a delay of 1 ps. The vertical cross sections of the associated reflectivity, phase, and absorption values are included in a plot where the local fluence is indicated, along with simulated values from the MRE model described above. By processing sets of images like those shown in Fig. 4 for different delays, it is possible to access the temporal evolution of the reflectivity, phase, and absorption for a given local fluence.

The images clearly show the excellent spatial resolution of the two imaging (reflectivity and interferometry) setups used. In the upper row, the selected images show the most relevant events associated with the excitation/relaxation of the surface over the corresponding time scales. For short delays (300 fs, 1 ps), a highly reflective and dense plasma is formed at the surface [23,24], corresponding approximately to the final temporal position indicated in the simulation in Fig. 3(a). A few picoseconds later (not included in the simulation), the reflectivity drops at the center of the excited region, indicating the onset of the ablation process [24,45,46]. In the tens to hundreds of picoseconds scale, the observed characteristic ring structure (*Newton rings*) indicates the expansion of a transparent layer of reduced density, and refractive index, with sharp interfaces [45]. It is worth noting that this ring structure has seldom been observed in fs-resolved imaging experiments in dielectrics, since its visibility requires a considerable refractive index contrast between the non-excited material and the ablating layer, as well as a sufficient spatial resolution to resolve the structure [47].

In reflectivity, phase, and absorption profiles, it can be seen that while the high reflectivity plasma density region (reflectivity at 400 nm above that of the unperturbed material, over-critical density) has a radius of $\sim$20 μm, the phase shift and absorption cross sections show that the electron plasma spreads beyond this zone, up a to radius $\sim$40 μm but with *subcritical* density [15], consistent with the lower local excitation fluence. A somewhat similar behavior has also been observed in Refs. [23,48], where transient transmission changes are clearly observed at lower local fluences than reflectivity changes.

A. Excitation and relaxation dynamics in fused silica

The corresponding transient reflectivity, phase shift and absorption plots for fused silica at different local fluences are shown in Fig. 5. The upper plot shows the phase shift evolution for a fluence well below the ablation threshold, indicating the temporal position of the excitation pulse. The measured phase signal in this case is associated with the instantaneous Kerr effect induced by the pump pulse (800 nm) and experienced by the probe pulse (400 nm)

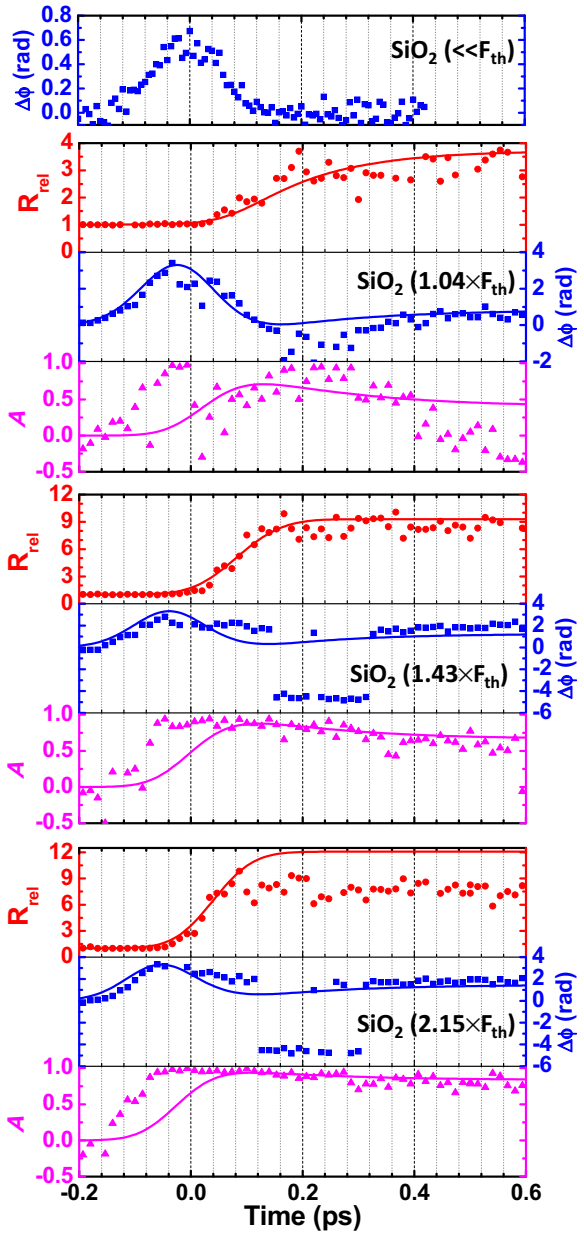

FIG. 5. Relative reflectivity at 400 nm (red), phase change (blue), and absorption (magenta) as a function of time upon excitation of fused silica at fluences well below F_{th} and at 1.04, 1.43, and 2.15 × F_{th}. The probe is s-polarized. Zero delay corresponds to the maximum of the 120 fs (FWHM) excitation pulse. The continuous lines are numerical simulations of the material response using the MRE model described in the text.

($S_{\text{Kerr}} \propto \int_{-\infty}^{+\infty} I_{\text{pump}}^2(t) \cdot I_{\text{probe}}(t-\tau) \cdot d\tau$). Its FWHM (145 ± 5 fs) allows calculating, after deconvolution with respect to the pump pulse temporal distribution and assuming a Gaussian temporal shape, a duration of the probe pulse as 115 ± 5 fs FWHM.

The noisy behavior of the curves is related to the large bandgap of the two materials analyzed, since even small changes of pulse energy and duration (pulse breathing, for instance) give rise to large changes in the amount of energy coupled in the material via multiphoton excitation at 800 nm. This effect is particularly visible in the reflectivity and absorption measurements for plasma densities close to n_{crit}, leading to relatively large fluctuations of the measured values. At this point it must be emphasized that each data point is the result of a single pump-probe measurement, and thus the time scans are a series of single pulse measurements, each at a fresh sample location for a given delay value. The scatter of the data points is thus directly representative of the peak intensity fluctuations of the laser source. Given the nonlinear nature of the interaction, we have preferred to not average the effect of multiple pulses for a given delay.

The interferometry measurements are in general less scattered, since the phase shift associated with the optical Kerr effect scales linearly with the pulse peak power and because the phase shift measurement averages values throughout the sample. However, for large plasma densities (i.e., high reflectivity values) at short delays, the very low transient transmission of the probed region, combined with the strong phase change across the spatially resolved cross section, leads to artifacts in the determination of absorption and phase.

At 1.04 × F_{th}, reflectivity increases after the peak of the excitation pulse, reaching a plateau value with a relative reflectivity $R_{\text{rel}} \sim 3.0$ in 150–200 fs. This value, according to our MRE calculations, is consistent with the formation of a thin electron plasma at the surface with a density around $10^{22}\,\text{cm}^{-3}$ and skin penetration depth of around a 100 nm [24,26]. When comparing the evolution of the reflectivity with that of the phase and the estimated absorption at this low fluence, there are several notable aspects. First, laser-induced changes already occur in the leading edge of the pump pulse in the phase and absorption transients, as opposed to what we can observe in the reflectivity measurements. This is not surprising since the phase shift before dense plasma formation is, as indicated above, sensitive to the Kerr effect induced by the pump pulse. In the case of absorption, we attribute its early increase, when compared with that of reflectivity, to the coherent coupling of the pump and probe pulses during temporal overlap, which depletes the probe pulse energy via third-order nonlinear optical susceptibility effects [49]. In this respect, it is worth noting that time-resolved transmission measurements performed in several dielectrics excited with fs laser pulses similarly show transmission decays much faster than the reflectivity rise, even for subablative fluences [22,24].

When the carrier density increases sufficiently, the phase shift departs from the Kerr-type response due to the negative sign contribution of free electrons and decreases to reach negative values some 250 fs after the pulse maximum. For delays beyond 350–400 fs, the phase recovers positive values, indicating the formation of self-trapped excitons, as widely shown by Mouskeftaras *et al.* [13] and Quéré *et al.* [15] in fused silica. The plasma density at the surface will not appreciably decrease, though, before several picoseconds.

There is thus an apparent contradiction between the reflectivity evolution and the phase and absorption values for delays beyond ∼350 fs for the lowest fluence analyzed. The reflectivity indicates that a dense (high reflectivity) plasma remains at the surface, while the phase shift indicates that the plasma has fully relaxed via STE formation and the absorption starts to decrease. The explanation for this apparent inconsistency is given by the different material

volumes interrogated by each measurement. For the reflected probe beam, the skin depth [26] of the surface plasma (at $\lambda = 400$ nm) for a carrier density on the order of 10^{21} cm^{-3} is about $\sim$20 μm. However, the skin depth is reduced by more than three orders of magnitude (down to $\sim$100 nm) for a plasma density just a factor of 10 higher (10^{22} cm^{-3}), assuming a scattering rate proportional to the plasma density [24,26]. In this case, the reflected probe pulse interrogates a very thin layer at the surface, much shallower than the region interacting with the transmitted probe, for delays in the hundreds of femtoseconds range and larger.

For fluences above and well above the ablation threshold (1.43 and 2.15 $\times$ F_{th} in Fig. 5), the reflectivity increases faster, reaching a plateau level ($R_{\text{rel}} \sim 8.5$) for both fluences in approximately 50 and 100 fs, respectively, after the maximum of the pulse. This indicates that a carrier density high enough for forming a strongly absorbing and reflecting plasma (over-critical density at the probe wavelength) is reached in a shorter time, consistent with the higher local fluence leading to a faster ionization rate. The higher fluences involved in this case also cause plasma formation signatures to be evident before the pump pulse maximum in the absorption and phase curves.

As a consequence of the strong electric field of the pump pulse around zero delay, the probe absorption measurements cannot be attributed alone to the material properties due to the coherent coupling of the pump and probe pulses. The rapidly growing plasma density around the pulse peak also causes strong phase gradients leading to phase shift artifacts in the form of discontinuous jumps until a sufficiently long delay (300–350 fs) is reached. Also within this temporal window, depending on the pump fluence, the probe pulse can be completely absorbed in the area corresponding to the center of the pump pulse, such that no phase can be measured. The phase and absorption measurements do therefore not provide reliable values in this temporal window and must be taken as merely indicative of the presence of nonlinear or plasma driven effects. After this "obscuration" lapse, the STE formation signature (stable positive phase shift beyond 350 fs) is clearly observable, while absorption shows a slow decrease in the observed temporal window.

As for the lowest fluence case (Fig. 5, 1.04 F_{th}), the reflectivity of the thin plasma layer at the surface remains high for several picoseconds at higher pulse energies (1.43 and 2.15 $\times$ F_{th}). This observation is fully consistent with previous transient reflectivity experiments [22–25] and suggests that either STE formation is not visible in the thin, surface ablating layer, or STEs do not contribute to carrier relaxation at large carrier densities. A possible explanation for this change in the plasma dynamics at high electron densities is a shift of the resonant frequency of the STEs to lower energies at the surface [50]. This effect has been implemented in the numerical model (see Table I) and has the consequence of reducing the real part of the denominator in the second term of Eq. (1), generating a total higher imaginary contribution to the dielectric function, which would result in a higher reflectance. This, combined with the limitation of one exciton per unit cell versus 12 possible CB electrons, would hide the exciton signature in the highly excited surface. This scenario, however, does not allow us to explain the overall reflectivity behavior experimentally observed in the long term (>1 ps; as will be seen in Fig. 7 and Sec. IV C) in both fused silica and sapphire. For both materials, reflectivity drops to its initial value in about 10 ps. This time is much shorter than the expected exciton lifetime in fused silica [10], while there is no STE formation in sapphire. As a consequence, it is difficult to ascribe the transient evolution of the reflectivity and the phase shift in silica to the shift in the STE resonant frequency in the near-surface region.

Alternatively, Coulomb screening appears to be a more plausible explanation. In the case of silica, the bulk STE radius is $\sim$2 Å [51], just slightly larger than the interatomic distance and comparable to the carrier-carrier separation ($\sim$3 Å) corresponding to a plasma density of 10^{22} cm^{-3}. For a carrier separation similar to the exciton radius, multiple Coulombic interactions would screen the electron-hole attraction, impeding the formation of STEs (similar to what happens at the Mott transition) until the plasma density is sufficiently reduced [52].

We have included in Fig. 5 numerical simulations of the expected evolution of reflectivity, phase, and absorption using the model described in the previous section. The initial increase observed experimentally in absorption during temporal overlap of the pump and probe pulses is not captured by the model, since it is most likely related to coupled-field absorption, as indicated above. This phenomenon is not included in the model. Yet, the simulations fit very well the reflectivity value at the plateau and the phase shift after the "obscuration" period (>350 fs), except for the highest fluence (2.15 F_{th}), for which the experimentally observed saturation value at the plateau ($R_{\text{rel}} \sim 8.5$) is not reproduced by MRE calculations. The experimentally observed saturation level of the reflectivity at the plateau, as discussed in the description of Fig. 3, is consistent with a scattering rate proportional to the plasma density that limits the reflectivity accessible to the free electron plasma due to carrier-carrier collisions [see the black trajectory in Fig. 3(a)]. The discrepancy of the computed reflectivity at the plateau observed in the simulations at the highest fluence is related to the necessity of the model to describe a large variation of electron distributions at different fluences, as discussed in Ref. [27].

In summary, our simultaneous space and time reflectivity and interferometric measurements in fs laser excited silica clearly show that the discrepancies previously observed in separately performed reflectivity and interferometric measurements are caused by the different volumes probed by the two techniques. Additionally, it has been shown that STE formation does not contribute to relaxation of the highly dense carrier plasma present at the ablating layer. Plasma relaxation in the layer underneath, exhibiting a much lower carrier density, occurs via STE formation over a time scale of few hundreds of femtoseconds. The deactivation of the STE relaxation mechanism at the surface ablating layer is most likely caused by Coulombic interactions that screen the electron-hole attraction at high carrier densities ($\sim 10^{22}$ cm^{-3}), impeding the formation of STEs.

B. Excitation and relaxation dynamics in sapphire

Evolution of the reflectivity, phase, and absorption for fluences of 1.02, 1.6, and 3.0 $\times$ F_{th} for sapphire is shown in

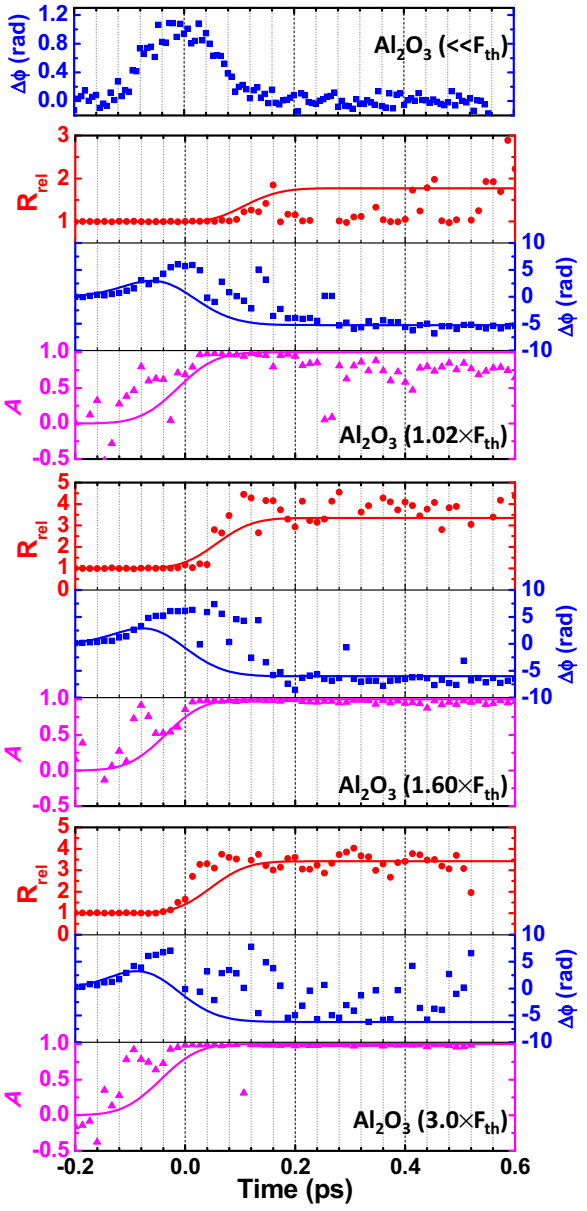

FIG. 6. Normalized reflectivity at 400 nm (red), phase change (blue), and absorption (magenta) as a function of time upon excitation of sapphire with fluences of 1.02, 1.60, and 3.0 × F_{th}. The probe is *s*-polarized. The zero delay corresponds to the maximum of the 120 fs (FWHM) excitation pulse. The continuous lines are numerical simulations of the material response (see text).

Fig. 6. For the lowest fluence shown (1.02 × F_{th}), the larger number of photons involved in the nonlinear ionization process combined with the threshold behavior of the reflectance makes small energy/pulse duration fluctuations clearly visible, with pulses of slightly different energy leading to under- or slightly over-critical plasma densities. Indeed, very small changes in the fluence (∼10%) around the ablation threshold value (F_{th}) have been observed to produce craters with large depth differences, ranging from an ∼5 nm (gentle ablation via Coulomb explosion [36,37,53]) to ∼100 nm (strong ablation). The overall evolution of the phase shift at 1.02 × F_{th} shows a behavior similar to that widely reported for subablative fluences in sapphire [13,15]. It is characterized by a decrease, after the Kerr effect peak, to negative values associated with the generation of carriers, leading to a long-lasting negative phase evolution associated with a long-lived plasma in absence of relaxation via STEs.

For fluences above (1.60 × F_{th}) and well above (3.0 × F_{th}) the ablation threshold, the reflectivity reaches a plateau with a fluence independent value (R_{rel} ∼ 3.5). The difference in the relative reflectivity values when compared with silica are caused by the higher refractive index and thus initial reflectivity of sapphire. As discussed for fused silica, in this regime, collisional excitation dominates over strong-field excitation. This causes [see Fig. 3(a)] a cooling of the CB electrons. When a lower temperature limit is reached, due to the Fermi velocity limit, the scattering rate becomes proportional to the density of free electrons, which makes the reflectance constant according to the Drude-Lorentz model. According to Fig. 3, the final reflectivity value reached corresponds to a free electron density of ∼5 × 10^{22} cm^{-3} at 1.6 × F_{th}.

The plasma buildup time in the reflectivity evolution for these high fluences does not show appreciable differences compared with fused silica, while the difference in the relative reflectivity plateau value compared with fused silica is caused by its larger initial reflectivity and is thus only apparent, as indicated above. As discussed for fused silica, the observation of the faster absorption increase with respect to reflectivity is related to the coherent coupling of the pump and probe beams during temporal overlap. Later, the generation of a sufficient density of free carriers originates an "obscuration" window at short delays (∼350 fs), during which phase-shift measurements are not reliable and are only indicative of Kerr and plasma driven effects, not yet observable in reflectivity.

As indicated above, the noisy signal in the phase shift measurements for short delays is caused by the difficulties in tracking the phase changes when the gradient is steep compared with the pixel separation on the spectrometer CCD. The obscuration window extends beyond 500 fs for the largest fluence studied (3.0 × F_{th}). In no case, as expected, is the positive phase shift signature of STEs observed in sapphire.

The continuous lines in Fig. 6 show the simulated evolution of reflectivity, phase, and absorption according to the MRE model. The simulation for 1.6 × F_{th} is the one also used in Fig. 3, where the instantaneous scattering rate and CB density are shown. A strong experimental indication of the validity of a model using a temperature-dependent scattering rate is the absence of any reflectivity dip below the initial value, unlike the prediction of the simple model with a scattering rate directly proportional to the carrier density [see Fig. 3(b)]. For the reflectivity evolution shown in Fig. 5 (fused silica) and Fig. 6 (sapphire) no reflectivity dip is experimentally observed, consistent with the model. Interestingly, this behavior differs from that observed in the case of $LiNbO_3$ [9], where the indicated transient reflectivity dip for electron densities in the vicinity of the critical density is clearly observed. It is worth noting, though, that in our model, the reflectivity actually evolves [white trajectory in Fig. 3(a)] through a saddle point between two minima with relative reflectivities <1. This saddle point should be deeper in the case of $LiNbO_3$ given its higher refractive index (and reflectivity), explaining the transient reflectivity minimum experimentally observed.

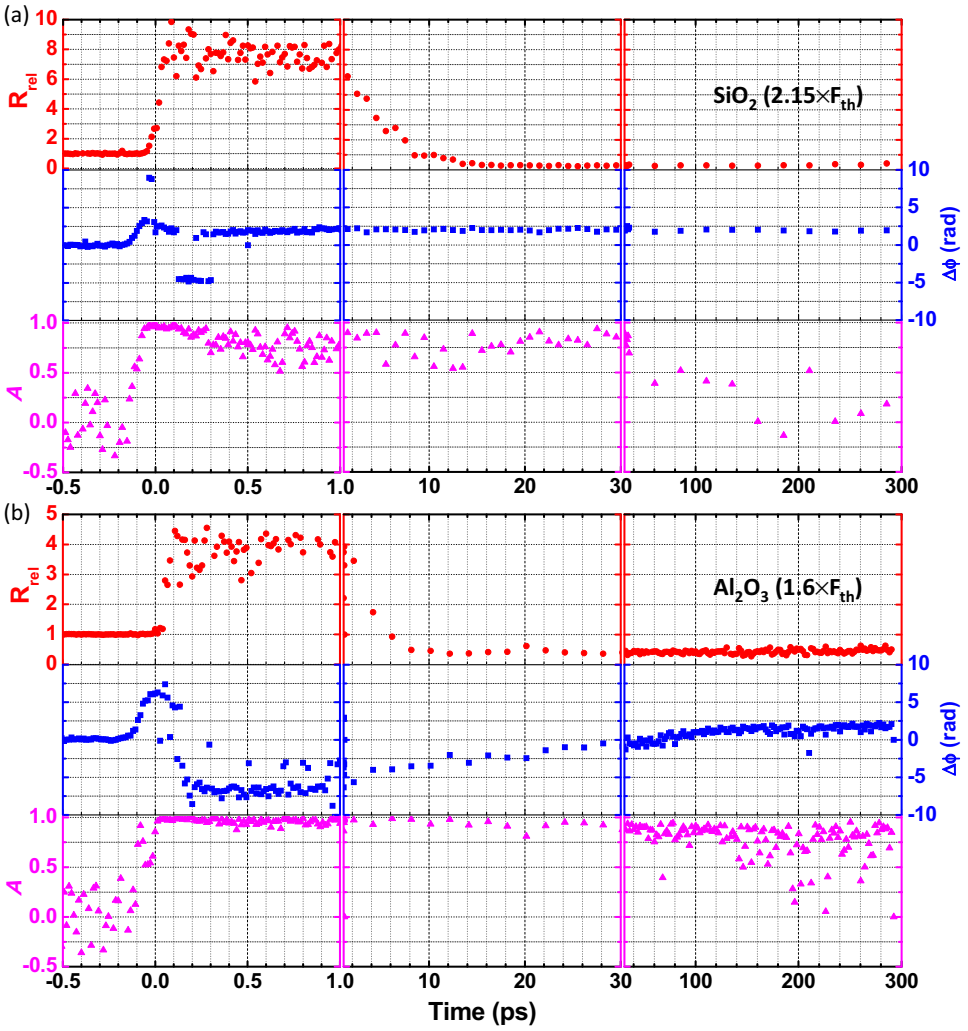

FIG. 7. Relative reflectivity at 400 nm (red), phase change (blue), and absorption (magenta) as a function of time upon excitation of silica (a) and sapphire (b), with a fluence of 2.15 × F_{th} and 1.6 × F_{th}, respectively. The probe is *s*-polarized in both cases. The zero delay corresponds to the maximum of the 120 fs (FWHM) excitation pulse.

C. Long-term evolution of reflectivity, phase, and absorption in fused silica and sapphire

Figure 7 shows the evolution of the reflectivity, phase, and absorption signals for fused silica and sapphire at fluences well above F_{th} over a time span of 300 ps. For both materials, we can distinguish three main regimes. The behavior in the short delay region (up to ∼1 ps) is essentially the one already described in Sections A and B.

In the intermediate delay range (1–30 ps), the reflectivity shows a decay to values below the initial level in ∼8–10 ps in both materials. This reflectivity drop has been identified with the onset of the ablation process in metals, semiconductors, and dielectrics [22,24,30,46] and is related, at least partly, to the transfer of excited carrier energy to the lattice via inelastic scattering. Such a reflectivity decrease has also been observed in other materials upon fs-laser-induced ablation [22,24,46] and attributed [22] to rapid structural damage at the surface, leading to scattering of the probe pulse, but without experimental evidence. This behavior could also be related to the extremely high temperature of the system right after carrier-lattice thermalization occurs, as discussed below. The material will stay in this low reflectivity state up to the maximum delay value recorded (30–300 ps interval). On the other hand, the phase shows a positive and stable value for intermediate (1–30 ps) and long delays (30–300 ps) for fused silica, in agreement with the long lifetime of STEs (400 ps to 1 ns, [10,54,55]).

For sapphire, a slow increase from negative phase values suggests that the excited material relaxes via slow processes, but here we also find a positive final phase shift and large absorption in the few hundreds of picoseconds range. This might indicate that at high excitation densities, some permanent defects are formed in the bulk of sapphire and modify its optical constants (as STEs do in silica). Thus, we might have two contributions to the relaxation: slow recombination in the moderately excited part of the probed region and a faster decay (not measurable here) due to defect formation close to the surface in the nonablated part. However, given the shallow thickness of this permanent layer (∼100 nm, [56]), the detection and identification of these defects by means of spectroscopic studies would require the use of a more sensitive technique (e.g., luminescence), which is out of the scope of this paper.

There is a temporal window (∼10–30 ps) during which both materials feature an interesting behavior, namely very low reflectivity and simultaneously high absorption (close to 1). This drop in reflectivity cannot be explained using Fig. 3. During the time scale for the reflectivity decrease (∼10 ps), a considerable transfer of energy from carriers to the lattice occurs and the assumptions behind the numerical model become invalid.

It is worth analyzing the origin of this behavior, showing a reflectivity drop down to values close to zero, also accompanied by negligible transmission values. We have to emphasize here that the time-resolved images of the surface in this delay range do not show any evidence of the presence of scattering centers. Indeed, the generation of surface roughness would imply the presence of a large number of local transverse gradients not present in a Gaussian beam profile, as well as mass flow or density fluctuations at unrealistic velocities. We can thus discard surface scatter as responsible for the strong reflectivity decay in the 10 ps time scale. Another plausible explanation might be the presence of a graded index in the expanding ablating layer. However, the observed phenomenon seems to be general and occurs not only in the two dielectrics analyzed here [47] but also, as indicated above, in fs-resolved imaging experiments in nontransparent materials like metals and semiconductors [46,57].

The observed low R and T values could have their origin in the expansion of a homogeneously excited and thermalized layer at the early stage of ablation. Following Ref. [58], it is worth noting that thermalization of carriers and lattice takes just a few picoseconds. At the end of the isochoric heating process, the material is an extremely hot solid (several thousand Kelvins) at a pressure of several tens of gigapascals. This heating stage is followed by the adiabatic expansion of the hot layer [58]. In the indicated time scale (∼10–30 ps), the expanding material does not have time to exchange a substantial amount of heat with the surrounding medium and might feature the optical properties of a high-temperature black body (negligible reflectivity, and absorptivity close to unity). Obviously, the confirmation of this speculative hypothesis would require a detailed assessment of the spectral properties of such a transient state of the material. However, a few arguments can be provided to motivate this interpretation and the origin and properties of such a transient "hot state".

The first argument is that similar reflectivity drops accompanied by negligible transmission values have been observed in other dielectrics [22,23]. Also, as recently shown in Ref. [47], the ablation process in dielectrics is preceded by the propagation of a rarefaction wave into the bulk, forming a layer with two parallel interfaces that separate with time, as similarly reported in semiconductors and metals [59]. The propagation of the wave takes place at the speed of sound, which brings this process into a time window close to that attributed to the formation of a hypothetical black body. We thus have two characteristic effects occurring in the same time window: the apparent behavior of the material as a transient black body and the adiabatic expansion accompanied by the propagation of a rarefaction wave inside the material. The nexus between both observations might be given by Wien's displacement law that describes the radiative behavior of a system with two interfaces in thermal equilibrium upon adiabatic expansion, a situation comparable with a thin (overheated or ablating) layer upon adiabatic expansion.

Obviously, additional mechanisms would need to be taken into account to fully describe the material behavior in the indicated time window, including, most likely, possible bandgap renormalization/shrinking effects prior to carrier-lattice thermalization, thermionic emission [60], as well as carrier diffusion [61]. Yet the similarity of the behavior observed here with that in numerous other dielectrics, even at subablative fluence [62], and the near-zero reflectivity in this delay window in metals and semiconductors suggest a common transient state, which could be that of a black body.

V. CONCLUSIONS

The results show that the apparent inconsistencies observed in previous works regarding the carrier relaxation dynamics measured by the two techniques are caused by the different volumes interrogated by each technique, especially at fluences near and above the ablation threshold.

We have shown that the reflectivity measurements are sensitive to the evolution of the plasma density in a very thin layer at the surface and at densities in the near-critical range. In turn, the interferometric measurements yield plasma density estimations averaged over an interaction volume, much larger than the skin depth of the dense plasma still present at the surface for fluences above the ablation threshold.

Comparison of the reflectivity and phase shift evolution in fused silica at the subpicosecond scale indicates that either STEs are not formed at large carrier densities or the presence of STEs cannot be distinguished from the plasma contribution to the reflectivity of the thin, ablating layer due to an energy shift of the exciton resonant frequency. STE formation signatures are observed, though, in the subablative layer underneath (exhibiting a much lower carrier density) in the phase measurements. Although the formation of excitons in the near-surface region, with a binding energy lower than in the bulk, would yield a reflectivity evolution consistent with the experimentally observed behavior, exciton formation within the ablating layer is most likely blocked by Coulomb screening for carrier densities in which carrier-carrier separation is on the order of the exciton radius.

For both materials, silica and sapphire, and for fluences well above the ablation threshold, the maximum measured plasma reflectivity shows a saturation behavior. Our numerical simulations show that in this high fluence regime, for the pulse duration used (120 fs FWHM), collisional excitation dominates over strong-field excitation. This causes a cooling of the CB electrons down to the Fermi velocity limit, where the carrier-carrier scattering rate becomes proportional to the density of free electrons. As a consequence, the reflectance of the excited surface becomes nearly constant according to the Drude-Lorentz model.

Finally, the behavior of both materials in the temporal window (∼10–30 ps), featuring simultaneously low reflectivity (close to zero) and high absorption (close to one), suggests that following isochoric heating and, for a short time lapse, before the excited region substantially expands or exchanges heat with the surroundings, the material transiently behaves optically like a high-temperature blackbody.

ACKNOWLEDGMENTS

This work has been partly funded by Laserlab-Europe (Grant Agreement No. 284464, EU's Seventh Framework Programme, Project No. SLIC002014), by the Spanish Ministry of Economy and Competiveness (Project No. TEC2014-52642-C2-1-R) as well as by the Danish Council for Independent Research | Natural Sciences. M.G.-L. acknowledges the FPU (Formación de Profesorado Universitario) Grant No. AP2012-0217 awarded by the Spanish Ministry of Education.

M.G.-L. and L.H.-L. equally contributed to the results presented in the paper.

[1] B. C. Stuart, M. D. Feit, S. Herman, A. Rubenchik, B. Shore, and M. Perry, Phys. Rev. B **53**, 1749 (1996).

[2] W. Kautek, J. Krüger, M. Lenzner, S. Sartania, C. Spielmann, and F. Krausz, Appl. Phys. Lett. **69**, 3146 (1996).

[3] M. Lenzner, J. Krüger, S. Sartania, Z. Cheng, C. Spielmann, G. Mourou, W. Kautek, and F. Krausz, Phys. Rev. Lett. **80**, 4076 (1998).

[4] B. Rethfeld, Phys. Rev. Lett. **92**, 187401 (2004).

[5] Z. Lin and L. V. Zhigilei, Phys. Rev. B **73**, 184113 (2006).

[6] P. Balling and J. Schou, Rep. Prog. Phys. **76**, 036502 (2013).

[7] B. Rethfeld, S. Linden, L. Englert, M. Wollenhaupt, L. Haag, C. Sarpe-Tudoran, and T. Baumert, Proc. SPIE **7005**, 70050O (2008).

[8] G. M. Petrov and J. Davis, J. Phys. B. At. Mol. Opt. Phys. **41**, 025601 (2008).

[9] M. Garcia-Lechuga, J. Siegel, J. Hernandez-Rueda, and J. Solis, J. Appl. Phys. **116**, 113502 (2014).

[10] D. Grojo, M. Gertsvolf, S. Lei, T. Barillot, D. M. Rayner, and P. B. Corkum, Phys. Rev. B **81**, 212301 (2010).

[11] M. Lebugle, N. Sanner, N. Varkentina, M. Sentis, and O. Utéza, J. Appl. Phys. **116**, 063105 (2014).

[12] A. Q. Wu, I. H. Chowdhury, and X. Xu, Phys. Rev. B **72**, 085128 (2005).

[13] A. Mouskeftaras, S. Guizard, N. Fedorov, and S. Klimentov, Appl. Phys. A Mater. Sci. Process **110**, 709 (2012).

[14] L. Huang, J. P. Callan, E. N. Glezer, and E. Mazur, Phys. Rev. Lett. **80**, 185 (1998).

[15] F. Quéré, S. Guizard, P. Martin, G. Petite, O. Gobert, P. Meynadier, and M. Perdrix, Appl. Phys. B **68**, 459 (1999).

[16] V. V. Temnov, K. Sokolowski-Tinten, P. Zhou, and D. von der Linde, J. Opt. Soc. Am. B **23**, 1954 (2006).

[17] C. V. Shank, R. Yen, and C. Hirlimann, Phys. Rev. Lett. **50**, 454 (1983).

[18] M. C. Downer, R. L. Fork, and C. V. Shank, J. Opt. Soc. Am. B **2**, 595 (1985).

[19] P. Martin, S. Guizard, P. Daguzan, G. Petite, P. D'Oliveira, P. Meynadier, and M. Perdrix, Phys. Rev. B **55**, 5799 (1997).

[20] S. Mao, F. Quéré, S. Guizard, X. Mao, R. E. Russo, G. Petite, and P. Martin, Appl. Phys. A Mater. Sci. Process **79**, 1695 (2004).

[21] F. Quéré, S. Guizard, and P. Martin, Europhys. Lett. **56**, 138 (2001).

[22] I. H. Chowdhury, A. Q. Wu, X. Xu, and A. M. Weiner, Appl. Phys. A Mater. Sci. Process **81**, 1627 (2005).

[23] D. Puerto, W. Gawelda, J. Siegel, J. Bonse, G. Bachelier, and J. Solis, Appl. Phys. A Mater. Sci. Process **92**, 803 (2008).

[24] D. Puerto, J. Siegel, W. Gawelda, M. Galvan-Sosa, L. Ehrentraut, J. Bonse, and J. Solis, J. Opt. Soc. Am. B **27**, 1065 (2010).

[25] J. Hernandez-Rueda, D. Puerto, J. Siegel, M. Galvan-Sosa, and J. Solis, Appl. Surf. Sci. **258**, 9389 (2012).

[26] J. Siegel and J. Solis, in *Femtosecond Laser Micromachining: Photonic and Microfluidic Devices in Transparent Materials*, edited by R. Osellame, G. Cerullo, and R. Ramponi (Springer, Berlin, 2012), pp. 19–41.

[27] A. Rämer, L. Haahr-Lillevang, B. Rethfeld, and P. Balling, Opt. Eng. **56**, 011015 (2016).

[28] K. Wædegaard, D. B. Sandkamm, L. Haahr-Lillevang, K. G. Bay, and P. Balling, Appl. Phys. A Mater. Sci. Process **117**, 7 (2014).

[29] D. Strickland and G. Mourou, Opt. Commun. **56**, 219 (1985).

[30] J. Bonse, G. Bachelier, J. Siegel, and J. Solis, Phys. Rev. B **74**, 134106 (2006).

[31] K. Sokolowski-Tinten, J. Bialkowski, M. Boing, A. Cavalleri, and D. von der Linde, Phys. Rev. B **58**, R11805(R) (1998).

[32] M. D. Williams, J. S. Ford, and D. L. Andrews, J. Chem. Phys. **143**, 124301 (2015).

[33] Q. Sun, H. Jiang, Y. Liu, Z. Wu, H. Yang, and Q. Gong, Opt. Lett. **30**, 320 (2005).

[34] R. Trebino, K. W. DeLong, D. N. Fittinghoff, J. N. Sweetser, M. A. Krumbügel, B. A. Richman, and D. J. Kane, Rev. Sci. Instrum. **68**, 3277 (1997).

[35] J. M. Liu, Opt. Lett. **7**, 196 (1982).

[36] D. Ashkenasi, A. Rosenfeld, H. Varel, M. Wähmer, and E. E. B. Campbell, Appl. Surf. Sci. **120**, 65 (1997).

[37] R. Stoian, D. Ashkenasi, A. Rosenfeld, and E. E. B. Campbell, Phys. Rev. B **62**, 13167 (2000).

[38] B. H. Christensen and P. Balling, Phys. Rev. B **79**, 155424 (2009).

[39] K. Wædegaard, M. Frislev, and P. Balling, Appl. Phys. A Mater. Sci. Process **110**, 601 (2012).

[40] L. Haahr-Lillevang, K. Wædegaard, D. B. Sandkamm, A. Mouskeftaras, S. Guizard, and P. Balling, Appl. Phys. A Mater. Sci. Process **120**, 1221 (2015).

[41] F. R. McFeely, E. Cartier, L. J. Terminello, A. Santoni, and M. V. Fischetti, Phys. Rev. Lett. **65**, 1937 (1990)

[42] I. M. Burakov, N. M. Bulgakova, R. Stoian, A. Mermillod-Blondin, E. Audouard, A. Rosenfeld, A. Husakou, and I. V. Hertel, J. Appl. Phys. **101**, 043506 (2007).

[43] S. Zafar, K. A. Conrad, Q. Liu, E. A. Irene, G. Hames, R. Kuehn, and J. J. Wortman, Appl. Phys. Lett. **67**, 1031 (1995).

[44] C. B. Schaffer, A. Brodeur, and E. Mazur, Meas. Sci. Technol. **12**, 1784 (2001).

[45] K. Sokolowski-Tinten, J. Bialkowski, A. Cavalleri, and D. von der Linde, Appl. Surf. Sci. **127-129**, 755 (1998).

[46] K. Sokolowski-Tinten, J. Bialkowski, A. Cavalleri, M. Boing, H. Schueler, and D. von der Linde, Proc. SPIE **3343**, 46 (1998).

[47] M. Garcia, J. Siegel, J. Hernandez-Rueda, and J. Solis, Appl. Phys. Lett. **105**, 112902 (2014).
[48] K. J. Wædegaard, D. B. Sandkamm, A. Mouskeftaras, S. Guizard, and P. Balling, Europhys. Lett. **105**, 47001 (2014).
[49] S. L. Palfrey and T. F. Heinz, J. Opt. Soc. Am. B **2**, 674 (1985).
[50] J. Song, R. M. VanGinhoven, L. R. Corrales, and H. Jónsson, Faraday Discuss. **117**, 303, (2000).
[51] S. Ismail-Beigi and S. G. Louie, Phys. Rev. Lett. **95**, 156401 (2005).
[52] P. Nêmec, P. Malý, M. Nikl, and K. Nitsch, Appl. Phys. Lett. **76**, 2850 (2000).
[53] J. Hernandez-Rueda, J. Siegel, M. Galvan-Sosa, A. Ruiz de la Cruz, M. Garcia-Lechuga, and J. Solis, J. Opt. Soc. Am. B **32**, 150 (2015).
[54] S. Richter, F. Jia, M. Heinrich, S. Döring, U. Peschel, A. Tünnermann, and S. Nolte, Opt. Lett. **37**, 482 (2012).
[55] D. Wortmann, M. Ramme, and J. Gottmann, Opt. Express **15**, 10149 (2007).
[56] J. Hernandez-Rueda, J. Siegel, M. Garcia-Lechuga, and J. Solis, J. Opt. Soc. Am. B **31**, 1676 (2014).
[57] P. Kühler, D. Puerto, M. Mosbacher, P. Leiderer, F. J. Garcia de Abajo, J. Siegel, and J. Solis, Beilstein J. Nanotechnol. **4**, 501 (2013).
[58] B. Rethfeld, V. Temnov, K. Sokolowski-Tinten, S. I. Anisimov, and D. von der Linde, Proc. SPIE **4760**, 72 (2002).
[59] K. Sokolowski-Tinten, J. Bialkowski, A. Cavalleri, D. von der Linde, A. Oparin, J. Meyer-ter-Vehn, and S. I. Anisimov, Phys. Rev. Lett. **81**, 224 (1998).
[60] T. Y. Choi and C. P. Grigoropoulos, J. Appl. Phys. **92**, 4918 (2002).
[61] K. Sokolowski-Tinten, J. Bialkowski, and D. von der Linde, Phys. Rev. B **51**, 14186 (1995).
[62] M. Garcia-Lechuga, J. Solis, and J. Siegel, Appl. Phys. Lett. **108**, 171901 (2016).